StrucOpt manuscript No.
(will be inserted by the editor)

Design of band-gap grid structures

A. R. Diaz*, A. G. Haddow and L. Ma

Abstract This paper discusses issues related to designing band-gaps in periodic plane grid structures. Finite element analysis is used to solve the dynamic behavior of a representative unit cell and Bloch-Floquet theory is used to extend the results to the infinite structure. Particular attention is given to the addition of non-structural masses that are introduced as design variables. These are used to create desirable features in the dispersion diagram. Physical insight is presented into the optimal choice of locations where masses should be added and the results of several numerical examples are provided to highlight this and other features of how band-gaps can be created and located at desired frequency ranges. The effect of the skew angle of the underlying grid structure is also explored, as are mathematical refinements of the modelling of the beam elements and the rotational inertia of the added masses. A scaling feature between the size of the reducible and the irreducible reference cell is exploited and the manner in which this can simplify optimization approaches is discussed.

Key words Grids, phononic structures,band-gaps, periodic structures

1 Introduction

Structures exhibiting band-gaps prevent the propagation of waves at certain frequencies. These structures may be phononic (sonic) or photonic, depending on their band-gap frequency range. Sonic band-gap structures can be used as frequency filters and wave guides, while photonic band-gap structures have applications in optics and microwaves. Because of their potential use in emerging technologies, particularly those involving MEMS and optical devices, the study of band-gap structures is receiving significant attention in the current literature.

Band-gaps appear in many kinds of periodic structures. In this paper we investigate the presence of band-gaps in plane grid structures, i.e., plane structures made of intersecting beams which deflect in the plane perpendicular to the plane of the structure. The goal is to create and maximize band-gaps in such structures by adding non-structural masses at strategic locations of the grid, while retaining the periodicity of the structure. A standard optimization problem is formulated whereby optimal mass distributions are identified that maximize gaps above specific bands while limiting the amount of added material.

The literature dealing with photonic band-gaps is very extensive. The popular web site Photonic & Sonic Band-Gap Bibliography (Dowling and Everitt 2004) lists over 3000 articles on photonic band-gaps as of this writing. Work on sonic or phononic band-gaps is much less abundant, although the pace of activity in this area is increasing rapidly. In early work, a theoretical analysis of vibration in periodic plane grids was discussed by Heckel (1964). Heckel found bands of high attenuation and bands of no attenuation for bending-wave transmission through plane grids. In recent work related to the present paper, Martinsson and Movchan (2003), and Jensen (2003) studied in-plane wave propagation in two-dimensional (2D) periodic lattice structures, including 2D truss structures, plane frames and 2D mass-spring models. The authors showed that complete band-gaps exist for certain distributions of stiffness and mass and demonstrated how band-gaps can be created at low frequency ranges by introducing a local resonator into periodic structures. An optimization perspective has also been used to introduce band-gaps in materials with a periodic structure. In Cox and Dobson (1999, 2000), a gradient based optimization method and an evolution algorithm were used to produce band-gaps in 2D photonic crystals. In Sigmund (2001) and Sigmund and Jensen (2002, 2003), topology optimization techniques were used to optimize band-gaps in elastic materials and to create

Received: date / Revised version: date

A. R. Diaz, A. G. Haddow and L. Ma

Department of Mechanical Engineering, Michigan State University, East Lansing, MI 48824–1226, USA
e-mail: diaz@egr.msu.edu, haddow@egr.msu.edu

* *Corresponding author*

acoustic and optical wave guides. In preliminary research leading to this work, Ma *et al.* (2004) showed the existence of band-gaps in plane grids. Other authors have investigated the propagation of elastic waves in various structures, including Parmley *et al.* (1995) in mass chains, Kafesaki *et al.* (1995) and Vasseur *et al.* (1998) in composites, and Sigalas and Economou (1994) in plates.

In this paper we analyze the grid using a finite element model. The analysis of plane wave propagation in periodic structures using finite element methods has been discussed by Orris and Petyt (1974), who used finite element techniques to evaluate the phase constant associated with the normal modes and natural frequencies of a periodic structure. A finite element approach was also used by Langlet *et al.* (1995) to investigate plane acoustic wave propagation in periodic materials containing inclusions or cylindrical pores.

The rest of the paper is organized as follows: first, a simple one-dimensional example is used to introduce basic concepts in wave propagation in periodic structures. This is followed by the analysis of infinitely periodic plane grids. In Section 3 the focus is on the geometry of the problem while in Section 4 the emphasis is on vibration analysis and the derivation of the finite element model of the problem. The optimization problem is discussed in Section 5. Examples are included for illustration in Section 6, followed by concluding remarks that summarize the results in the last section of the paper.

2
Introductory Example

Before presenting the detailed theory and definitions associated with the analysis of the periodic grid and the optimization of its behavior, a simple 1-D example is presented that can be easily understood and analyzed, and yet can be generalized to more complex cases. It is hoped that this will help bridge the language barrier that is often encountered in the different disciplines engaging in research in this field. In this introductory example particular attention will be given to the physical interpretation of concepts such as band-gaps, filters, standing waves, mode shapes, and dispersion diagrams.

Fig. 1 shows a sketch of the introductory example to be analyzed in this section. It represents a structure comprised of a uniform beam with additional point masses m_1 and m_2 spaced a distance $L/2$ apart in an alternating fashion, as shown. The usual notation of *E, A, I, ρ*, is adopted for the beam and in this example values are assigned as E=30 GPa, A=15 mm^2, I=10 mm^4, L=100 mm, with the density $\rho = 3000$ kg/m^3. For simplicity a finite element model will be used based on standard 2-node, Euler-Bernoulli beam elements. Nodes are located at each point mass and transverse deflections and rotations are defined as in the figure. The structure has a spatial periodicity of L. There will be no intermediate nodes located between the non-structural masses. These

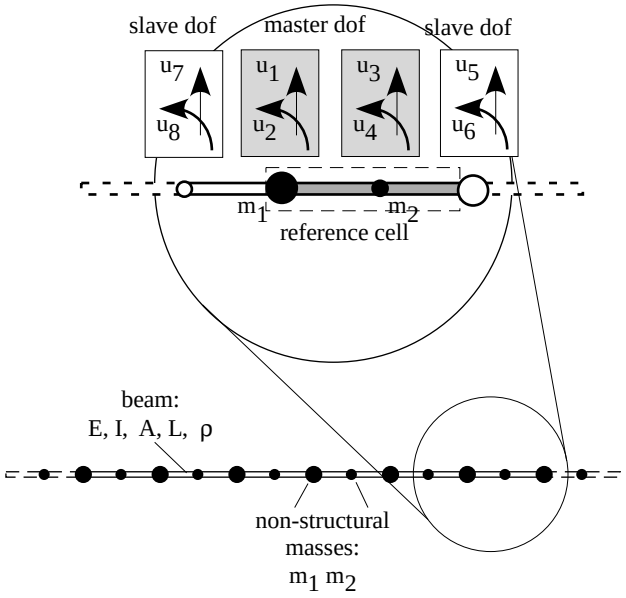

Fig. 1 Schematic of the introductory example

restrictions will be removed in later sections. Also, strict definition of terms will be postponed until that time as the main purpose in this section is to give a physical appreciation of the issues at hand.

The dynamic behavior of the infinite beam can be found by considering only the reference cell and making use of the Bloch-Floquet theory (Brillouin 1953)

$$\mathbf{u}^n = e^{ikn}\mathbf{u}^0 \tag{1}$$

This relates the deflections of any slave node $\mathbf{u}^n$ to the deflections of a master node in the reference cell, $\mathbf{u}^0$. The integer n describes the number of L translations to the right ($n > 0$) or to the left ($n < 0$). In the example of Fig. 1, one has:

$$\mathbf{u}^0 = \begin{pmatrix} u_1 \\ u_2 \\ u_3 \\ u_4 \end{pmatrix},$$

$$\mathbf{u}^1 = \begin{pmatrix} u_5 \\ u_6 \\ .. \\ .. \end{pmatrix} = \begin{pmatrix} u_1 \\ u_2 \\ .. \\ .. \end{pmatrix} e^{ik},$$

and

$$\mathbf{u}^{-1} = \begin{pmatrix} .. \\ .. \\ u_7 \\ u_8 \end{pmatrix} = \begin{pmatrix} .. \\ .. \\ u_3 \\ u_4 \end{pmatrix} e^{-ik}$$

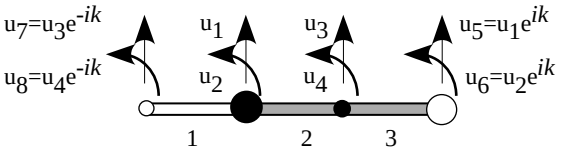

Fig. 2 Section of beam used to build finite element model

For clarity, the additional coordinates are not shown in the figure but could be numbered using an appropriate scheme. The real number k is referred to as the wave number and, as will be shown, is used to fix the wavelength of associated eigenvectors and the values of the eigenvalues. The way k determines the behavior of the system is key to a full appreciation of the general theme of this paper. In later sections the goal will be to tailor the distribution of the eigenvalues by the optimally sizing and positioning of some of the system's parameters.

In this example, the first mass will be set to four times the mass of each beam element, i.e., m_1=0.009 kg and m_2 will be set to zero. Using a standard finite element approach, the mass and stiffness matrices can be constructed in the usual manner and a four degree of freedom system of equations can be constructed and it is of the form:

$$\mathbf{M}\ddot{\mathbf{u}}^0 + \mathbf{K}\mathbf{u}^0 = \mathbf{0} \tag{2}$$

Stiffness $\mathbf{K}$ and mass $\mathbf{M}$ matrices are assembled from a three element segment of the infinite beam (Fig. 2). As all degrees of freedom in this segment are not independent, the kinematic constraints imposed by elements on either side of the reference cell appear in both $\mathbf{M}$ and $\mathbf{K}$ as terms including the factor $e^{\pm ik}$.

One can solve the eigenvalue problem arising from (2) for a given value of the wave number k. For each k there will be four eigenvalues $\lambda_p(k)$, $p = 1, 2, 3, 4$ and four eigenvectors. To obtain *all* possible values of $\lambda_p(k)$ one should consider all possible real values of k. However, because of the manner in which k appears in $\mathbf{M}$ and $\mathbf{K}$, always in the form $e^{\pm ik}$, $\mathbf{M}$ and $\mathbf{K}$ are 2π periodic and one need only explore wave numbers in the range $k \in [-\pi, \pi]$ to ensure that all solutions are found. Moreover, (2) is unchanged if k is replaced by $-k$, therefore all possible solutions can be generated by investigating the range $k \in [0, \pi]$. Having done this, Fig. 3 shows a plot of the natural frequencies $\omega_p = \sqrt{\lambda_p}/(2\pi)$ of the system as a function of the wave number. Plots such as this are known as dispersion diagrams. There are a number of important features to be aware of:

- Points where $\frac{d\omega}{dk} = 0$ correspond to stationary or standing waves, whereas for non zero gradients of ω, the corresponding eigenvectors generate solutions that describe travelling waves.
- In this example there exist regions where no eigenvalues are found. Physically, this means the structure acts as a filter to frequencies lying in this region. For example, with reference to Fig. 3, if a time dependent forcing term where added to the right hand side of (2) with a frequency in the range [$\omega_1(\pi)$,$\omega_2(\pi)$], no wave would propagate through the structure. The region(s) where no eigenvalues exist - regardless of the wave number - are called band-gap(s). Creating such gaps and then optimizing the design of the structure to maximize the width of these gaps is central to the purpose of this paper.

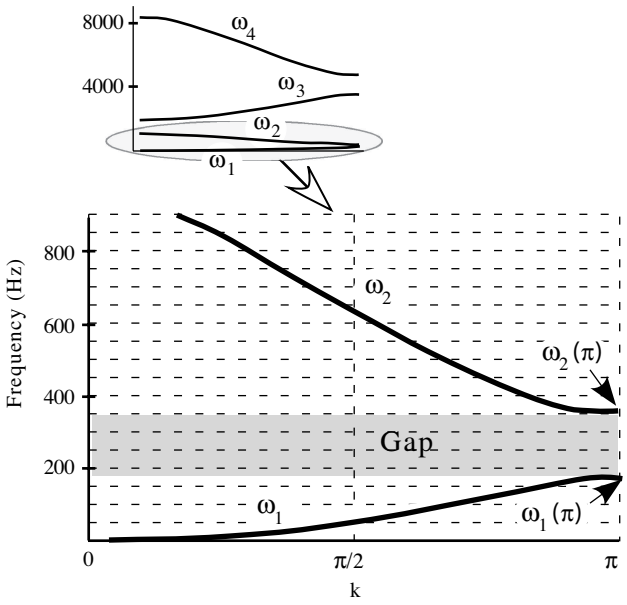

Fig. 3 The dispersion diagram for m_1=0.009 kg and m_2=0

To close this introductory section we will highlight one issue involved in creating band-gaps. Assume that our goal is to distribute the non-structural masses (m_1 and m_2) in such a way as to maximize a gap. In general, one would expect a complicated interaction between different frequency bands as various mass distributions are explored. However, consider the standing waves associated with the natural frequencies that bound the gap shown in Fig. 3: the lower band maximum value of ω_1= 200 Hz at k=π and the upper band minimum value of ω_2= 395 Hz, also at k=π. The two modes associated with these eigenvalues, plotted over the length of the reference cell, are shown in Fig. 4. For the mode associated with $\omega_2(\pi)$ there is no motion at the location of m_1 ($x = 0$ and $x = L$). Therefore, $\omega_2(\pi)$ is not influenced by m_1 and increasing m_1 will not lower the second band. The situation with the lower frequency mode is completely reversed: this mode is *greatly* influenced by m_1, since it moves through a maximum displacement at x=0. In a sense, there has been an uncoupling of the sensitivity of the upper band minimum to the amount of m_1 added. It is now only influenced by m_2. The opposite is true for the lower band maximum. This interplay between the wave number, standing waves, critical points in the band-gap,

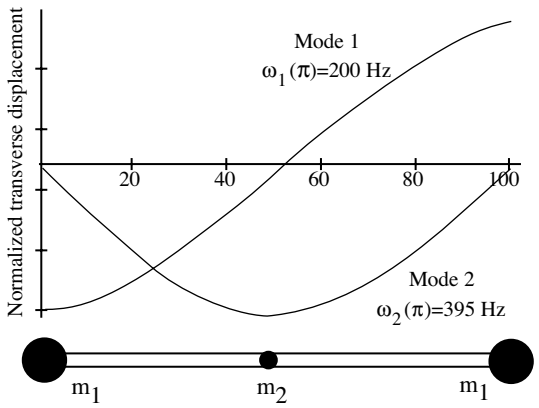

Fig. 4 The two lowest modes of the reference cell

and the optimal mass distribution will be further discussed in subsequent sections.

We now move on to the 2D problem involving plane grids, the subject matter of this paper.

3
Geometry of the periodic grid structure

A *periodic* plane grid Ω^p is a plane grid that can be constructed by periodically repeating a sub-section Ω of the grid through translations along two non-collinear vectors $\mathbf{t}^{(1)}$ and $\mathbf{t}^{(2)}$, i.e.,

$$\Omega^p = \bigcup_{\mathbf{n}\in \mathrm{Z}^2} (\Omega + n_1\mathbf{t}^{(1)} + n_2\mathbf{t}^{(2)}), \quad n_1, n_1 \in \mathrm{Z}$$

Integers n_1 and n_2 measure cell translations along the *tiling vectors* $\mathbf{t}^{(1)}$ and $\mathbf{t}^{(2)}$, respectively (Fig. 5). Ω is called a *representative* cell of the periodic grid. An *irreducible* cell is the smallest representative cell capable of tiling Ω^p through this tiling process. An arbitrary cell $\Omega^{\mathbf{n}}$ in the periodic grid can be identified simply by its cell number $\mathbf{n}=(n_1, n_2)^T$ as $\Omega^{\mathbf{n}}= \Omega + \mathbf{Tn}$, where $\mathbf{T} = [\mathbf{t}^{(1)}, \mathbf{t}^{(2)}]$. For the representative cell Ω, $\mathbf{n}=(0,0)^T$.

In this paper we only consider cells that are contained exactly in the parallelepiped spanned by the tiling vectors. This is not a severe limitation, as it can be shown that any polygonal cell that tiles the plane can be replaced by an equivalent parallelepiped (Diaz and Benard 2001). In this case the corners of the cells $\Omega^{\mathbf{n}}$ define the *direct lattice* of the periodic grid. This is the set

$$L = \{\mathbf{x} \in \mathrm{R}^2 : \mathbf{x} = \mathbf{Tn},\, \mathbf{n} \in \mathrm{Z}^2\}$$

The direct lattice characterizes the periodicity of the grid, which in turn introduces constraints on the shape of the waves that can propagate through the structure.

Using Bloch-Floquet theory (Brillouin 1953), the vibration properties of Ω^p can be extracted from the analysis of an irreducible representative cell Ω. In this paper, this analysis will be based on a finite element model, i.e., Ω is represented as a collection of nodes and elements. Nodes that belong to a single cell are labelled *master nodes*. A master node in an arbitrary cell $\Omega^{\mathbf{n}}$ can be identified by a cell number $\mathbf{n}$ and a node index j and is a member of the set $M_{\mathbf{n}} = \{(\mathbf{n}, j)\}_{j=1}^{NMN}$, where NMN is the number of master nodes in the representative cell. Note that if $(\mathbf{0}, j)$ is a master node in Ω, then the master node $(\mathbf{n}, j)$ in $\Omega^{\mathbf{n}}$ is an image of $(\mathbf{0}, j)$.

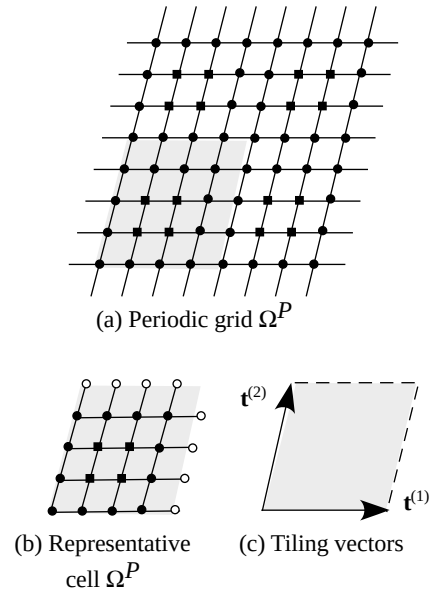

Fig. 5 Infinite 2D periodic grid structure

Master nodes in the representative cell are displayed as filled dots and squares in Fig. 5(b). To facilitate analysis, additional nodes are added to the representative cell to account for the mass and stiffness of the elements connecting to neighboring cells. These additional nodes are *slave nodes* and are denoted by the void dots in Fig. 5(b).

4
Vibration analysis of the periodic grid

4.1
Quasi-periodicity

Let $\mathbf{u}^{(\mathbf{0},j)}$ denote the (generalized) displacements of master node $(\mathbf{0}, j)$ in Ω. Applying Bloch-Floquet theory, the displacements of master node $(\mathbf{n}, j)$ in $\Omega^{\mathbf{n}}$ can be expressed as

$$\mathbf{u}^{(\mathbf{n},j)} = e^{i\hat{\mathbf{k}}\mathbf{Tn}}\mathbf{u}^{(\mathbf{0},j)} \tag{3}$$

where $\hat{\mathbf{k}} = (\hat{k}_1, \hat{k}_2)$ is the *wave vector*. After setting

$$k_1 = (\hat{\mathbf{k}} \cdot \mathbf{t}^{(1)}) \text{ and } k_2 = (\hat{\mathbf{k}} \cdot \mathbf{t}^{(2)}) \tag{4}$$

(3) can be expressed more simply as

$$\mathbf{u}^{(\mathbf{n},j)} = e^{i\mathbf{k}\cdot\mathbf{n}}\mathbf{u}^{(\mathbf{0},j)} \tag{5}$$

where $\mathbf{k} = (k_1, k_2) \in \mathrm{R}^2$ and k_1, k_2 may be interpreted as changes in phase of a wave between a cell and its neighboring cells along translation vectors $\mathbf{t}^{(1)}$and $\mathbf{t}^{(2)}$, respectively.

Let $\mathbf{u}^m \in \mathrm{C}^{NMD}$ and $\mathbf{u}^s \in \mathrm{C}^{NSD}$ be the displacement vectors associated, respectively, with master and slave nodes of the representative cell. Here *NMD* and *NSD* denote the number of degrees of freedom associated, respectively, with master and slave nodes in the cell (note that $\mathbf{u}^m \equiv \left\{\mathbf{u}^{(\mathbf{0},j)}\right\}_{j=1}^{NMN}$). Since slave nodes in the representative cell are master nodes in the cell's neighbors, applying (5) to all slave nodes in the representative cell permits $\mathbf{u}^s$to be expressed in terms of $\mathbf{u}^m$ as

$$\mathbf{u}^s = \mathbf{B}\mathbf{u}^m \tag{6}$$

where $\mathbf{B} \in \mathrm{C}(NSD,NMD)$. $\mathbf{B}$ is called here the *quasi-periodicity matrix*. Clearly, $\mathbf{B}$ depends on the wave vector $\mathbf{k}$. Since slave nodes in Ω are members of $\Omega^{(1,0)^T}$ or $\Omega^{(0,1)^T}$, $\mathbf{B}$ has *only* entries that are either 0, 1, e^{ik_1}, or e^{ik_2}.

4.2 Stiffness and mass matrices for a 2D grid representative cell

A standard finite element model is used here to model the grid. The element used is a two-node, three degree of freedom per node element, with degrees of freedom as follows: translation perpendicular to the grid plane, rotation to account for out of plane bending, and rotation about the longitudinal axis of the element. Bending is modelled using either Euler-Bernoulli or Timoshenko assumptions. Joints at points of intersection of the grid are assumed to be rigid and one or more elements are used to model each segment between two adjacent intersections. Consistent mass matrices are used in the analysis.

The stiffness and mass matrices of a representative cell, respectively $\mathbf{K}^c$ and $\mathbf{M}^c$, can be constructed following a standard finite element assembly procedure. After partitioning of the cell's degrees of freedom $\mathbf{u}^c \in \mathrm{C}^{NMD+NSD}$ as $\mathbf{u}^c = \{\mathbf{u}^m, \mathbf{u}^s\}^T$, these matrices are expressed as

$$\mathbf{K}^c = \begin{bmatrix} \mathbf{K}^{mm} & \mathbf{K}^{ms} \\ \mathbf{K}^{sm} & \mathbf{K}^{ss} \end{bmatrix} \tag{7}$$

and

$$\mathbf{M}^c = \begin{bmatrix} \mathbf{M}^{mm} & \mathbf{M}^{ms} \\ \mathbf{M}^{sm} & \mathbf{M}^{ss} \end{bmatrix} \tag{8}$$

Matrices $\mathbf{K}^c$ and $\mathbf{M}^c$ are real, symmetric and sparse but the degrees of freedom associated with these matrices are not independent. Using (6), $\mathbf{K}^c$ and $\mathbf{M}^c$ can be reduced so that the resulting equations of motion are expressed only in terms of the master degrees of freedom. This is described in detail in the following section.

4.3 Equations of motion

The kinetic energy (T) and potential energy (V) of the representative cell can be expressed as

$$T = \frac{1}{2}(\dot{\mathbf{u}}^c)^*\mathbf{M}^c\dot{\mathbf{u}}^c \tag{9}$$

$$V = \frac{1}{2}(\mathbf{u}^c)^*\mathbf{K}^c\mathbf{u}^c \tag{10}$$

Here $()^*$denotes Hermitian transpose. In view of the periodicity of the structure, $\mathbf{u}^m$ and $\mathbf{u}^s$ are not independent degrees of freedom and therefore, the energy expressions (9) and (10) involve a non-minimal set of generalized coordinates. We seek mass and stiffness matrices such that kinetic and potential energies in one cell are expressed in terms of *only* $\mathbf{u}^m$, i.e., matrices $\mathbf{M}$ and $\mathbf{K}$ such that

$$T = \frac{1}{2}(\dot{\mathbf{u}}^m)^*\mathbf{M}\dot{\mathbf{u}}^m \tag{11}$$

$$V = \frac{1}{2}(\mathbf{u}^m)^*\mathbf{K}\mathbf{u}^m \tag{12}$$

Using (8), (9) can be written in matrix form as

$$T = \frac{1}{2}[(\dot{\mathbf{u}}^m)^*, (\dot{\mathbf{u}}^s)^*] \begin{bmatrix} \mathbf{M}^{mm} & \mathbf{M}^{ms} \\ \mathbf{M}^{sm} & \mathbf{M}^{ss} \end{bmatrix} \begin{bmatrix} \dot{\mathbf{u}}^m \\ \dot{\mathbf{u}}^s \end{bmatrix}$$

Since $\mathbf{u}^s = \mathbf{B}\mathbf{u}^m$ and $\mathbf{B}$ is not a function of time, it follows that

$$T = \frac{1}{2}[(\dot{\mathbf{u}}^m)^*, (\mathbf{B}\dot{\mathbf{u}}^m)^*] \begin{bmatrix} \mathbf{M}^{mm} & \mathbf{M}^{ms} \\ \mathbf{M}^{sm} & \mathbf{M}^{ss} \end{bmatrix} \begin{bmatrix} \dot{\mathbf{u}}^m \\ \mathbf{B}\dot{\mathbf{u}}^m \end{bmatrix}$$

or

$$T = \frac{1}{2}(\dot{\mathbf{u}}^m)^*(\mathbf{M}^{mm} + \mathbf{B}^*\mathbf{M}^{sm} + \mathbf{M}^{ms}\mathbf{B} + \mathbf{B}^*\mathbf{M}^{ss}\mathbf{B})\dot{\mathbf{u}}^m$$

from which the definition of $\mathbf{M}$ follows:

$$\mathbf{M} = \mathbf{M}^{mm} + \mathbf{B}^*\mathbf{M}^{sm} + \mathbf{M}^{ms}\mathbf{B} + \mathbf{B}^*\mathbf{M}^{ss}\mathbf{B} \tag{13}$$

Similarly, from (7), (10) and (12), the stiffness matrix $\mathbf{K}$ is

$$\mathbf{K} = \mathbf{K}^{mm} + \mathbf{B}^*\mathbf{K}^{sm} + \mathbf{K}^{ms}\mathbf{B} + \mathbf{B}^*\mathbf{K}^{ss}\mathbf{B} \tag{14}$$

The equations of motion of the representative cell are therefore

$$\mathbf{M}\ddot{\mathbf{u}}^m + \mathbf{K}\mathbf{u}^m = \mathbf{f} \tag{15}$$

where $\mathbf{f}$ is a vector of generalized forces.

4.4 The dispersion diagram

Assuming a time-harmonic form of wave propagation in the periodic structure, let

$$\mathbf{u}^m = \mathbf{a}e^{i\omega t} \tag{16}$$

where ω is the wave vibration frequency and $i = \sqrt{-1}$. Letting $\mathbf{f} = \mathbf{0}$ in (15) leads to the eigenvalue problem

$$(\mathbf{K} - \lambda\mathbf{M})\mathbf{a} = \mathbf{0} \tag{17}$$

where $\lambda{=}\omega^{\mathbf{2}}$ is an eigenvalue and $\mathbf{a} \in \mathrm{C}^{NMD}$ is the corresponding eigenvector. Note that because of the presence of the quasi-periodicity matrix $\mathbf{B}$ in (13) and (14), $\mathbf{M}$ and $\mathbf{K}$ are functions of the wave vector $\mathbf{k} = (k_1, k_2)$ and therefore both λ and $\mathbf{a}$ depend on $\mathbf{k}$. As discussed in the introductory example, a *dispersion diagram* displays bands of eigenfrequencies as functions of the wave vector, where each *band* is associated with a given mode (this was illustrated in Fig. 3). In principle, in order to draw this diagram, equation (17) should be solved for each $\mathbf{k} \in \mathrm{R}^2$. However the periodicity of the structure results in significant simplifications. In fact, all eigenfrequencies on the periodic structure are produced by exploring only a small subset of R^2. This leads to the concept of *reciprocal lattice*.

The set of all wave vectors $\hat{\mathbf{k}}$ that yield waves with the same periodicity of the direct lattice L is known as the *reciprocal lattice* L_R. This lattice can be described using two tiling vectors $\mathbf{d}^{(1)}$ and $\mathbf{d}^{(2)}$, as the set

$$L_R = \{\hat{\mathbf{k}} \in \mathrm{R}^2 : \hat{\mathbf{k}} = m_1\mathbf{d}^{(1)} + m_2\mathbf{d}^{(2)}, \quad (m_1, m_2) \in \mathrm{Z}^2\}$$

where $\mathbf{d}^{(1)}$ and $\mathbf{d}^{(2)}$ are the solution to

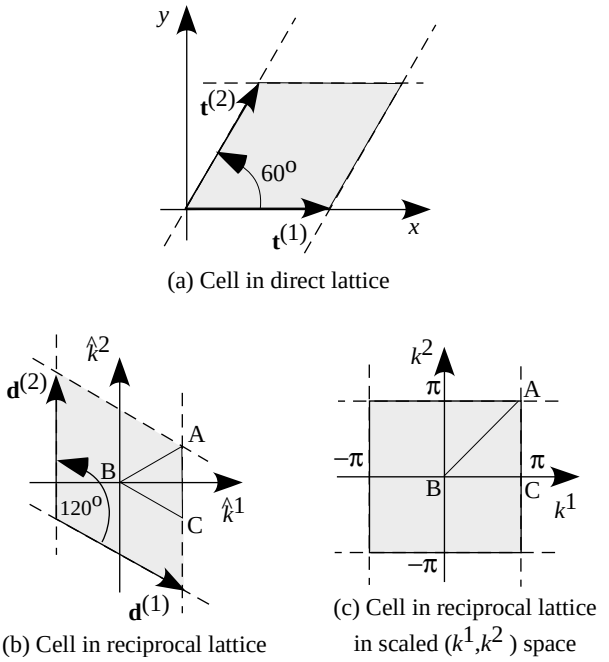

Fig. 6 A cell in the direct lattice and its corresponding cell in the reciprocal lattice

$$\mathbf{t}^{(i)} \cdot \mathbf{d}^{(j)} = 2\pi\delta_{ij} \tag{18}$$

for i, j=1, 2. In view of (3), a wave vector $\hat{\mathbf{k}}$ belongs to L_R provided that $e^{i\hat{\mathbf{k}}\mathbf{x}} = e^{i\hat{\mathbf{k}}(\mathbf{x}+\mathbf{X})}$ for any $\mathbf{x} \in L$ and all $\mathbf{X} \in L$. This implies that $\hat{\mathbf{k}} \in L_R$ if $e^{i\hat{\mathbf{k}}\mathbf{X}} = 1$ for all $\mathbf{X} \in L$ that is, if the product $\hat{\mathbf{k}}\mathbf{Tn}$ is a multiple of 2π for all integer vectors $\mathbf{n}$. Since the function $e^{i\hat{\mathbf{k}}\mathbf{Tn}}$ has the periodicity of the reciprocal lattice, equation (3) indicates that modes $\mathbf{u}^{(\mathbf{n},j)} = e^{i\hat{\mathbf{k}}\mathbf{Tn}}\mathbf{u}^{(\mathbf{0},j)}$ are also periodic in the $(\hat{k}_1, \hat{k}_2)$ plane and have the same periodicity of the reciprocal lattice. Therefore, all eigenfrequencies can be obtained by solving (17) using *only* values of $\hat{\mathbf{k}}$ in one cell of the reciprocal lattice. This is the first Brillouin zone (Brillouin 1953). It is easy to show that using the scaled values of the wave vectors $\mathbf{k} = \hat{\mathbf{k}} \cdot \mathbf{T}$, the first Brillouin zone (Fig. 6(b)) is mapped into the square $[-\pi, \pi]^2$ in the (k_1, k_2) plane. Therefore, all solutions to the eigenvalue problem (17) can be obtained even if $\mathbf{k}$ is evaluated only on the square $[-\pi, \pi]^2$ (Fig. 6 (c)). For a given structure, the j-th band in the dispersion diagram, associated with the j-th mode, is the set

$$b_j = \{\omega_j(\mathbf{k}) : \mathbf{k} \in [-\pi, \pi]^2\} \tag{19}$$

Waves of frequency ω such that $\omega \notin b_j$for *any* j do not propagate in the structure and hence the structure has a band-gap at ω. The goal of the optimization problem set up in the next chapter is to widen these gaps by a judicious modification of the structure.

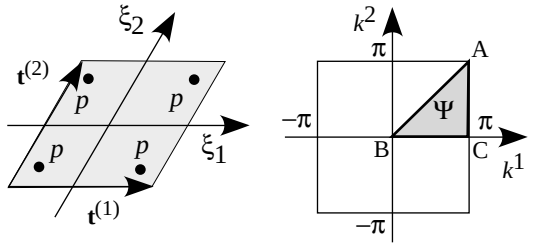

(a) A symmetric material distribution in the direct lattice

(b) Region of the first Brillouin zone explored

Fig. 7 Region of the (k_1, k_2) space explored if grid is symmetric within Ω

4.5 Further Simplifications

It is possible to show that *all* frequencies in b_j in (19) can be obtained even when a smaller subset of the (k_1, k_2) plane is explored. For instance, it is easy to show that the mass and stiffness matrices $\mathbf{M}$ and $\mathbf{K}$ (see (13) and (14)) are invariant with respect to transformations $(k_1, k_2) \mapsto (-k_1, -k_2)$ within the first Brillouin zone. Therefore, if $\mathbf{a}(\mathbf{k})$ is a mode with eigenfrequency ω, so is $\mathbf{a}(\text{-}\mathbf{k})$. As a result, the j-th band can be obtained simply by searching in the upper-half of the Brillouin zone, i.e.,

$$b_j = \{\omega_j(\mathbf{k}) : \mathbf{k} \in [-\pi, \pi] \times [0, \pi]\}$$

To account for this and perhaps other simplifications, we define Ψ as a subset of $[-\pi, \pi]^2$ such that *all* solutions $\lambda = \omega^2$ to the eigenvalue problem (17) are obtained whenever b_j is defined as

$$b_j = \{\omega_j(\mathbf{k}) : \mathbf{k} \in \Psi\} \tag{20}$$

One additional simplification is possible when the grid has certain symmetries within the irreducible cell Ω. Suppose p is a parameter that affects $\mathbf{K}^c$ and $\mathbf{M}^c$ in (7) and (8) (e.g., density, elastic modulus, nodal coordinates, etc) and let the spatial variation of p within Ω be expressed using a local set coordinates (ξ_1, ξ_2) measured along the tiling vectors $\mathbf{t}^{(1)}$ and $\mathbf{t}^{(2)}$ with origin at the center of Ω (Fig. 7(a)). If $p(\xi_1, \xi_2)$ is symmetric under the transformations $(\xi_1, \xi_2) \mapsto (-\xi_1, \xi_2)$, $(\xi_1, \xi_2) \mapsto (\xi_1, -\xi_2)$, and $(\xi_1, \xi_2) \mapsto (\xi_2, \xi_1)$, then all solutions of (17) are invariant with respect to the transformations $(k_1, k_2) \mapsto (-k_1, k_2)$, $(k_1, k_2) \mapsto (k_1, -k_2)$ and $(k_1, k_2) \mapsto (k_2, k_1)$ within the zone $[-\pi, \pi]^2$. In such cases the set Ψ in (20) is reduced to the triangle enclosed by corners at (π, π),(0,0),$(\pi, 0)$ (Cox and Dobson 1999) as depicted in Fig. 7(b).

5 Optimization problem

In this section we formulate an optimization problem to create and maximize band-gaps in 2D periodic grids by adding non-structural, lumped masses at strategic locations. Design variables x_i in the optimization problem control the magnitude of the lumped mass added at the $i-$th design location(s), D_i. In the present formulation, lumped masses are added only at master nodes and one variable may control the magnitude of masses added to more than one node. Lumped mass x_i affects directly the translation degree of freedom of the affected node(s). In addition, in order to account for the possibility that the additional mass also affects the rotational inertia of the structure, the mass matrices are modified by adding $f_{\phi_y} x_i$ and $f_{\phi_x} x_i$ to the diagonal entries associated with *rotational* degrees of freedom ϕ_x, and ϕ_y of the affected nodes. Parameters f_{ϕ_x} and f_{ϕ_y} are prescribed for each problem.

If a gap exists above the j-th mode, the gap's size is measured by the function

$$G(\mathbf{x}) = \min_{k \in \Psi} \omega_{j+1}(\mathbf{k}, \mathbf{x}) - \max_{k \in \Psi} \omega_j(\mathbf{k}, \mathbf{x}) \tag{21}$$

In (21) ω_j and ω_{j+1} are, respectively, the $j-$th and $(j+1)$-th eigenfrequencies associated with problem (17). Clearly, a gap exists above mode j if and only if $G(\mathbf{x})>0$. The optimization problem to be solved is: Find $\mathbf{x} \in \mathrm{R}^n$ that

$$\begin{aligned} &\text{maximizes } G(\mathbf{x}) = \min_{k \in \Psi} \omega_{j+1}(\mathbf{k}, \mathbf{x}) - \max_{k \in \Psi} \omega_j(\mathbf{k}, \mathbf{x}) \\ &\text{subject to} \qquad 0 \le x_i \le x_{\max} = \beta * m_{ref} \end{aligned} \tag{22}$$

In this problem n is the number of design variables and β and $x_{\max}$ are prescribed positive real numbers that control the total amount of nonstructural material that can be added to the cell and m_{ref} is a representative scaling parameter, e.g., the magnitude of the structural mass of the representative cell.

5.1 Numerical implementation of the optimization problem

To solve problem (22) numerically, the set Ψ in (21) is replaced by a discrete set $\hat{\Psi}$ of m sample points, e.g., the set

$$\hat{\Psi} = \{\mathbf{k}^1, \mathbf{k}^2, \cdots, \mathbf{k}^m\} \tag{23}$$

for $\mathbf{k}^p \in \Psi$. For fixed $\mathbf{x}$, this introduces discrete estimates of gap sizes evaluated at wave vectors $\mathbf{k}^p$ and $\mathbf{k}^q$ in $\hat{\Psi}$. Gap sizes between bands j and $j+1$ are estimated by

$$\hat{G}(\mathbf{x}) = \max_{1\le p,q\le m} G_{pq}(\mathbf{x})$$

where the $p \times q$ functions $G_{pq}(\mathbf{x})$ are defined as

$$G_{pq}(\mathbf{x}) = \omega_{j+1}(\mathbf{k}^p, \mathbf{x}) - \omega_j(\mathbf{k}^q, \mathbf{x}) \tag{24}$$

for p, q= 1,..., m and $\mathbf{k}^p$, $\mathbf{k}^q \in \hat{\Psi}$. In computations, (22) is replaced by: Find $\mathbf{x} \in \mathrm{R}^n$ that

$$\begin{aligned} &\text{maximizes } \hat{G}(\mathbf{x}) = \max_{1\le p,q\le m} G_{pq}(\mathbf{x}) \\ &\text{subject to} \qquad 0 \le x_i \le x_{\max} = \beta * m_{ref} \end{aligned} \tag{25}$$

If for a given $\mathbf{x}$ the solutions $\mathbf{k}_j^*$ and $\mathbf{k}_{j+1}^*$ to the min and max problems in (21) belong to $\hat{\Psi}$, $G(\mathbf{x}) = \hat{G}(\mathbf{x})$. In *particular*, if this is the case for the *optimal* $\mathbf{x}$, then the solution to (25) is also a solution to (22). Otherwise, the solution to (25) is only an approximation to the optimal solution, but one that can be improved by increasing the size of $\hat{\Psi}$.

Problem (25) can be written in a form that is more suitable to numerical optimization as: Find $\mathbf{x} \in \mathrm{R}^n$ and $z \ge 0$ that

$$\begin{aligned} &\text{maximize } z \\ &\text{subject to } G_{pq}(\mathbf{x}) = \omega_{j+1}(\mathbf{k}^p, \mathbf{x}) - \omega_j(\mathbf{k}^q, \mathbf{x}) \ge z \\ &\qquad 0 \le x_i \le x_{\max} = \beta * m_{ref} \end{aligned} \tag{26}$$

This problem is solved numerically using the method of moving asymptotes, MMA (Svanberg 1987). This requires gradients of the constraints, which are obtained by standard sensitivity analysis, as described next.

5.2 Sensitivity analysis

The gradient of $G_{pq}(\mathbf{x})$ with respect to design variable $\mathbf{x}$ is computed using well-known formulas. Letting $(\cdot)'$ denote $\partial(\cdot)/\,\partial\mathbf{x}$,

$$G'_{pq} = (\omega_{j+1}(\mathbf{k}^p, \mathbf{x}))' - (\omega_j(\mathbf{k}^q, \mathbf{x}))' \tag{27}$$

where

$$2\omega_j\omega'_j = (\mathbf{a}^j)^*\mathbf{K}'\mathbf{a}^j - \lambda_j(\mathbf{a}^j)^*\mathbf{M}'\mathbf{a}^j \tag{28}$$

$\omega_j^2 = \lambda_j$ and $\mathbf{a}^j$ is normalized with respect to the mass matrix $\mathbf{M}$. This expression is valid provided that the eigenfrequencies ω_j are distinct at $\mathbf{x}$. In computations, one must be mindful of the potential difficulties caused by loss of differentiability at repeated eigenvalues. Fortunately, experience shows that these difficulties are overcome by the MMA algorithm.

In (28), λ_j and $\mathbf{a}^j$ can be obtained from the current design. Furthermore, $\mathbf{K}' = \mathbf{0}$ since adding non-structural masses does not change the stiffness of the structure. This leaves the computation of $\mathbf{M}'$, which is discussed next.

Suppose design variable x_i affects master nodes $m \in D_i$. As the added masses are lumped, $\mathbf{M}'$ is diagonal and has nonzero entries only at positions corresponding to the degrees of freedom of nodes $m \in D_i$, since x_i appears only at these locations. Therefore, from (28),

$$\frac{\partial\omega_j}{\partial x_i} = -\frac{\omega_j}{2}\sum_{m\in D_i}(\mathbf{a}_m^j)^*\mathbf{F}\mathbf{a}_m^j \tag{29}$$

where entries $\mathbf{a}_m^j$ represents the component in the mass-normalized eigenvector $\mathbf{a}^j$ corresponding to the degrees of freedom of node m and $\mathbf{F}$ is 3×3 is diagonal with diagonal entries $(1, f_{\phi_x}, f_{\phi_y})$ (recall that for each design variable x_i the mass matrix is modified by adding x_i, $f_{\phi_x}x_i$, and $f_{\phi_y}x_i$ to the affected degrees of freedom).

Once $\frac{\partial\omega_j}{\partial x_i}$ is computed using (29), the gradient $G'_{pq}$is be obtained from (27). To facilitate computations, an active set of strategy is introduced so that a sequence of problems is solved by considering only a *subset* of the most critical constraints in (26). To avoid introducing redundant constraints, at most n of the most critical constraints are kept each time (n represents the total number of design variables). As the algorithm converges, feasibility of the solution is verified against the *complete* set of constraints. A solution obtained this way is a Kuhn-Tucker point of the reduced problem and a feasible solution of (26) but possibly not a Kuhn-Tucker point. This is because solutions to (26) may not be regular points of the constraints and may violate constraint qualification conditions.

6 Examples

In the following examples we consider the design of grids characterized by representative cells Ω of different sizes, including those shown in Fig. 8. The beam sections are rectangular with cross section $b \times h = 2 \times 0.5$ mm with the wide side on the plane of the grid. Masses are placed symmetrically on Ω, at grid joints and also mid-side in each grid segment (each grid segment between two grid corners is discretized using two finite elements). The bound on the maximum allowable additional added mass is $x_{\max} = m_{ref}$ where $m_{ref} = 8\rho bhL_0$ and $L_0 = 10$ mm is the size of one grid segment. For simplicity, in what follows x is normalized by $x \to x/x_{\max}$ so that in re-

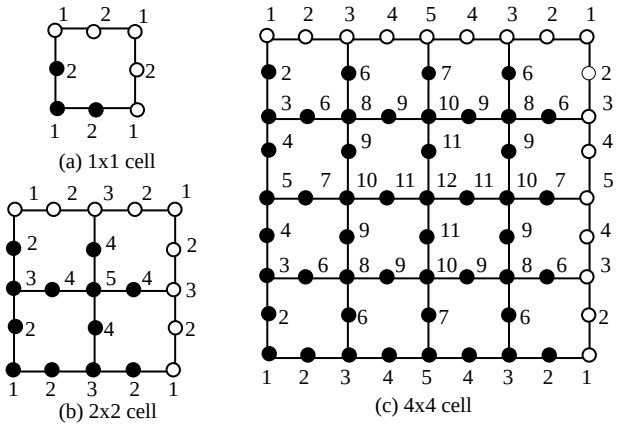

Fig. 8 Symmetric cells of different sizes showing locations for additional masses controlled by design variables

porting a solution, x=1 indicates that the upper bound constraint is active.

Except as discussed in Example 4, it is assumed that the addition of masses affects only the translation degrees of freedom, i.e., $f_{\phi_x} = f_{\phi_y} = 0$ in (29). The beam model used satisfies Euler-Bernoulli's assumptions, except in Example 5, where results are compared to solutions obtained for Timoshenko beam models. Material properties are: E=5.28*10^6 GPa, G=1.98*10^6 GPa and ρ=1200 kg/m^3. The section $\hat{\Psi}$ of the reciprocal lattice searched (see (23)) includes only points on the boundary of the triangle A-B-C in Fig. 7.This is the accepted practice in structures of this type and searching points *inside* the triangle is expected to yield no additional eigenvalues.

6.1 Example 1

This simple example will serve to illustrate the nature of solutions to the 2D problem. We seek to design a band-gap into the grid by adding masses in a symmetric arrangement characterized by a 2×2 *square* irreducible cell Ω of side $L = 2L_0 = 20mm$. The gap will be placed above the second band.

At the solution to this problem, the dispersion diagram is as shown in Fig. 9 (a). The gap appears above 34 kHz and extends to 68 kHz. The solution consists of simply adding the largest possible mass at design position 3 of the cell (mid-edge, Fig. 9(b)).

The optimal mass distribution can be explained by examining the modes at critical locations in the dispersion diagram. For example, the mode associated with the maximum eigenvalue of band 2, at point (0,0) of the dispersion diagram, achieves the maximum magnitude at design position 3 (Fig. 9(b)). Since adding masses at points with larger displacements introduces more substantial drops in the corresponding eigenvalue, adding a mass at position 3 is most effective at *lowering* band 2. Simultaneously, the mode associated with the *minimum* eigenvalue of band 3, at point (π,π) of the dispersion diagram, has a *node*, i.e., a location that has no out-of-plane motion, at design position 3. Hence, masses added at position 3 will not lower the critical point of band 3. Thus, by lowering the low band while keeping the high band unchanged, a mass placed at location 3 has the most impact of the size of the gap between the two bands. Quantitatively, from (27) and (29)

$$\frac{dG}{dx_3} = \tfrac{1}{2} \sum_{m \in D_3} (\omega_2 \left\| a_m^2 \right\|^2 - \omega_3 \left\| a_m^3 \right\|^2) = \tfrac{1}{2} \sum_{m \in D_3} \omega_2 \left\| a_m^2 \right\|^2 > 0$$

where $a_m^j, \quad m \in D_3$ are amplitudes of modes j=2,3 measured at design position 3. For this particular design $a_m^3 = 0$ at all four locations associated with position 3, insuring that $\frac{dG}{dx_3} > 0$, which explains why x_3 should be made as large as possible. A similar argument can be applied to design position 1, to conclude that no mass should be placed there since $\frac{dG}{dx_1} < 0$. While in general it is cumbersome to carry this analysis on to larger, more complex problems, the analysis does generate insights into the nature of solutions to this problem.

6.2 Example 2

In this example we seek to design a band-gap into the grid by adding masses in a symmetric arrangement characterized by a 4×4 irreducible cell of side $L = 4L_0$ =40 mm. We consider both a square and a skewed lattice with angles α=90° and α=60° and translation vectors $\mathbf{t}^{(1)} = (L, 0)^T$ and $\mathbf{t}^{(2)} = L(\cos\alpha, \sin\alpha)^T$. Gaps are introduced above bands 1, 2 and 5.

There are some general comments that can be made regarding the results of this example. In general, the way in which the mass is distributed around the reference cell is dictated by the mode shapes that are involved and the conflicting requirements of lowering the critical frequency of the lower band, while trying to increase the critical frequency of the upper band. If we wish to create a gap between bands 1 and 2, it is advantageous to add as much mass as possible close to the center of the reference cell, as doing this lowers the critical point of band 1 without a corresponding decrease in the critical point of band 2. The situation is similar when the gap is to be introduced above higher bands. A more quantitative analysis could be presented, similar to the approach using $\frac{dG}{dx_3}$ in Example 1, but for brevity it is omitted.

Note that the upper limit of additional mass $x_{\max}$ assigned in this example is not large enough to create a gap for the square reference cell yet it is enough to open a small gap for the skewed cell(see Fig. 10(a) and Fig.

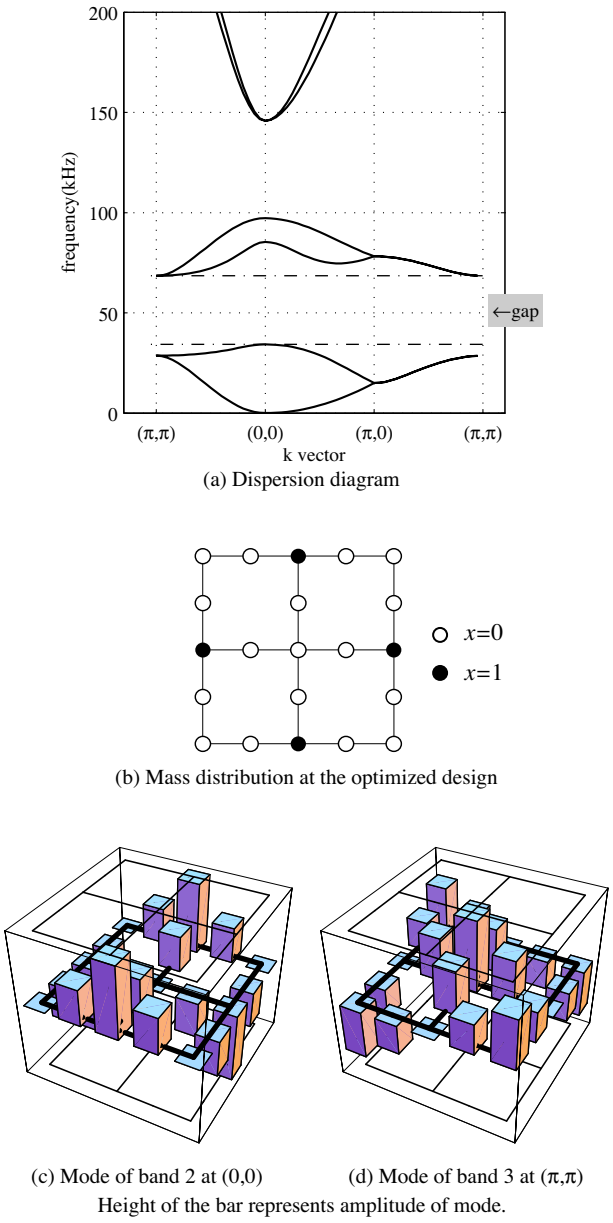

Fig. 9 Details associated with the solution of Example 1

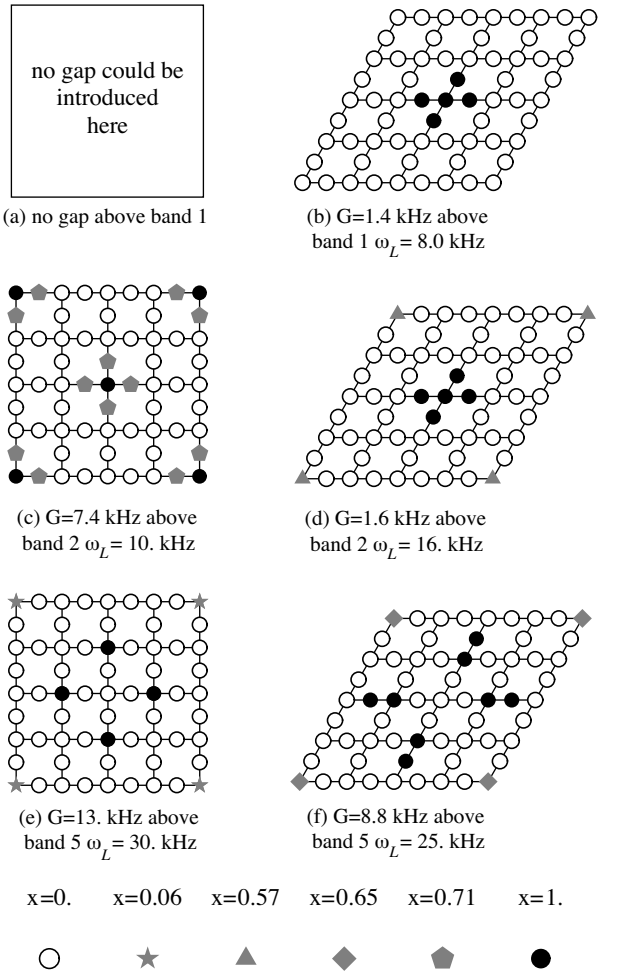

Fig. 10 Example 2: material distribution in optimized cell

10(b)). This will be discussed next, when the influence of the skew angle is investigated further.

To expand upon this example, we now study the influence of the skew angle of the lattice α on the size of the gap, for a variety of different cell sizes and gap locations. Cell sizes of 1×1, 2×2, and 4×4 are studied and gaps between bands 1 and 2 (G1) and bands 2 and 3 (G2) are sought. The results are depicted in Fig. 12. To facilitate the display of the results, we report the magnitude of the gap relative to the largest gap at any angle. This will be a quantity between 1 (locating the skew angle(s) where the gap is the largest) to 0 (which will indicate that there is no gap possible). Perhaps the most important point to note from these results is that the size of the gap does not always vary monotonically with the skewness of the cell, as illustrated in Fig. 12.

6.3 Example 3

In design applications one may be interested in creating a gap near a particular frequency. Here we discuss how this can be attempted *without changing material or section properties, or grid dimensions.* One alternative is to fix the scale of the problem by selecting the size of the irreducible cell - e.g., 4×4 - and proceed to solve several problems, each problem maximizing the gap above a different band. From the solutions obtained one then selects the one that best fits the design purpose. While there is no guarantee that a suitable band-gap in the desired frequency range will be found this way, this procedure results in designs which may then be scaled, if necessary, by scaling the material properties.

In order to understand the gap positioning problem better, it is useful to look into the effect of the size of the irreducible cell used in the analysis. If the tiling period of the mass distribution is characterized by a 1×1 irre-

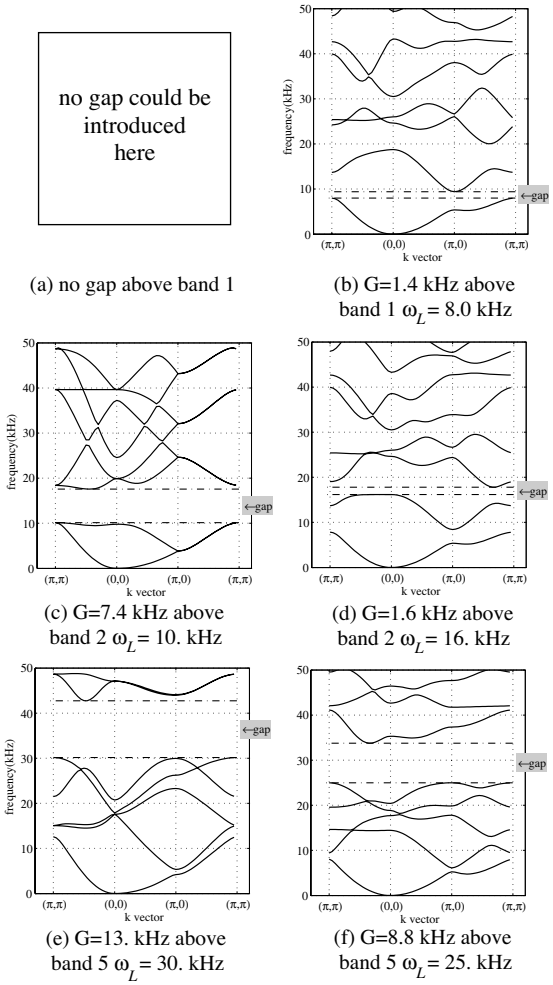

(a) no gap above band 1
(b) G=1.4 kHz above band 1 ω_L= 8.0 kHz
(c) G=7.4 kHz above band 2 ω_L= 10. kHz
(d) G=1.6 kHz above band 2 ω_L= 16. kHz
(e) G=13. kHz above band 5 ω_L= 30. kHz
(f) G=8.8 kHz above band 5 ω_L= 25. kHz

Fig. 11 Example 2: dispersion diagrams for solutions depicted in Fig. 10

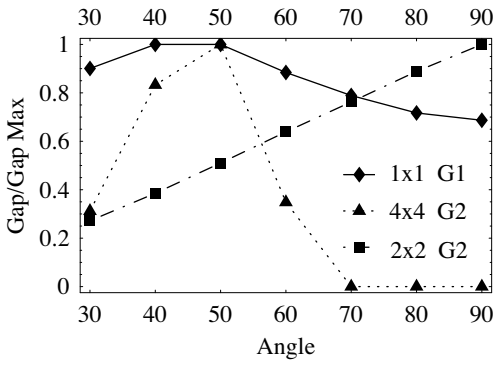

Fig. 12 Variation of the gap size with cell angle

ducible cell, optimal solutions of the problem have dispersion diagrams as shown in Fig. 13(a). The maximum gap above band 1 starts at $\omega_L = 50$ kHz and extends for 95 kHz. Design variables (scaled by $x_{\max}$) are $\mathbf{x}$=(1,0). If the *same* design were to be repeated over a 2×2 or a 4×4 patch of the grid (thus forming a *reducible* cell), the dispersion diagram would show exactly the same gap

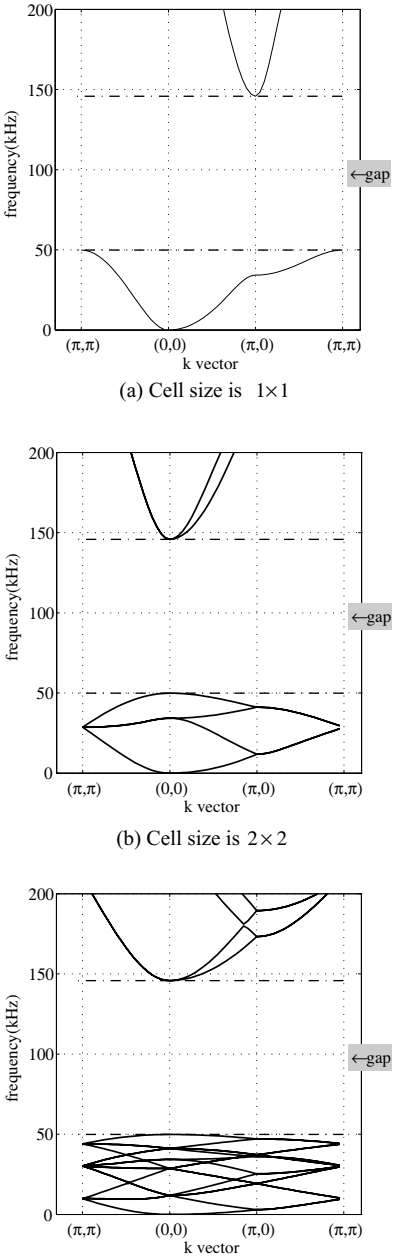

(a) Cell size is 1×1
(b) Cell size is 2×2
(c) Cell size is 4×4

Fig. 13 Dispersion diagrams for an optimized periodic material distribution analyzed using different reference cell sizes

in the same frequency range, but the gap would appear above a different band number. The gap appears above band 4 in the 2×2 and above band 16 in the 4×4 cell. This is illustrated in Fig. 13(b) and (c).

This suggests that, if one were interested in creating a gap above 50 kHz, one should consider a 1×1 periodic mass distribution, as larger cell periods will lead to *reducible* local optimal solutions. For frequencies below 50 kHz, larger cell size periods should be investigated. This analysis can proceed in sequence, looking at larger cell period sizes, one at a time. For example, a 2×2 irreducible periodic cell has at most three gaps that can

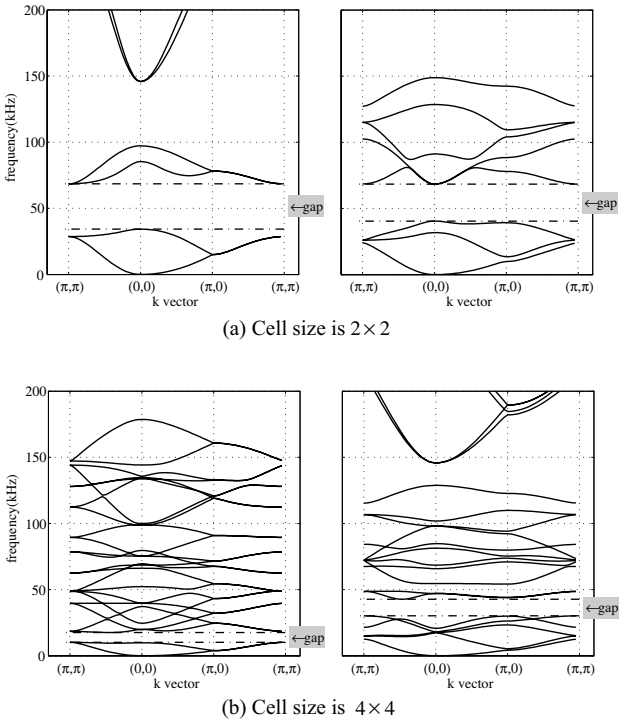

Fig. 14 Dispersion diagrams for optimized periodic material distributions with different periodicities

be maximized *and* start below 50 kHz, namely, bands 1, 2 and 3. For the present parameter bounds, no gap can be introduced above band 1. A gap of maximum size above band 2 starts at $\omega_L = 34$ kHz while a gap above band 3 starts at $\omega_L = 40$ kHz (Fig. 14 (a)). Thus, for frequencies of interest above 34 kHz but below 50 kHz a 2×2 cell should be investigated. This sequence can be continued for yet lower frequencies. The general rule is to investigate gaps above bands 1 to $4n$-1 of the larger cell when the immediately smaller cell has its *first* gap above band n. The 2×2 cell has its first gap above band 2 at 34 kHz. This suggests that a 4×4 cell period should be used for frequencies *below* 34 kHz, with focus on bands below the 8-th band. Two such solutions are displayed in Fig. 14(b), corresponding to gaps above bands 2 at 10 kHz and 5 at 30 kHz. The material layouts corresponding to all these solutions are shown in Fig. 15.

6.4
Example 4. Model refinements: effect of rotational inertia

In the previous examples the additional mass did not affect the rotational inertia of the structure, i.e., $f_{\phi_x} = f_{\phi_y} = 0$ (recall that for each design variable x_i the mass matrix is modified by adding x_i, $f_{\phi_x} x_i$, and $f_{\phi_y} x_i$ to the affected degrees of freedom). Here we explore briefly the effect of including rotational inertia in the analysis. In Fig. 16 we show the dispersion diagrams corresponding to solutions obtained in the previous section for 2×2

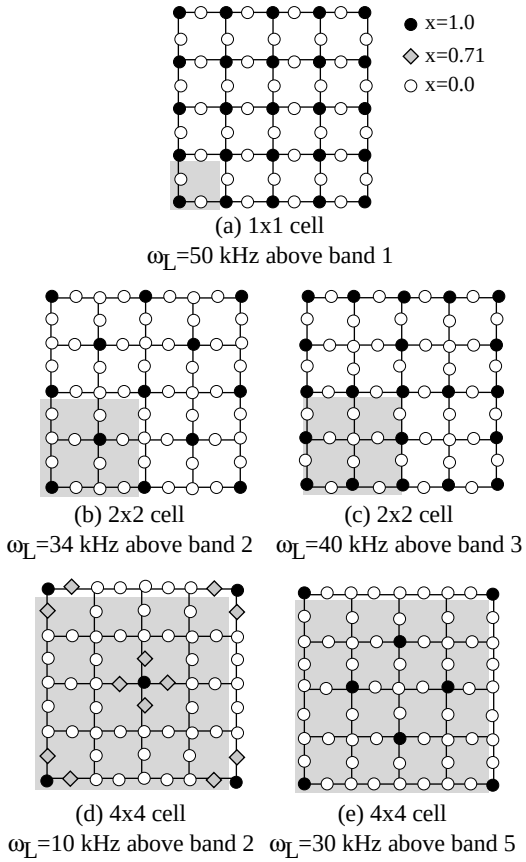

Fig. 15 Example 3: optimized solutions associated with different material periodicities

and 4×4 cells and compare these results with dispersion diagrams obtained using the same mass distribution but setting now $f_{\phi_x} = f_{\phi_y} = (2h)^2$. This would correspond to a point mass placed a distance $2h$ from the beam's neutral axis. The results indicate that for these values of the parameters including the rotational inertia has only a small effect on high frequency solutions and essentially no effect on low frequency solutions.

6.5
Example 5. Model refinements: effect of Timoshenko model

Experts in this field may object to the use of Euler-Bernoulli beam theory in this analysis, finding instead that a Timoshenko model is more suitable. By means of a couple of examples, here we expose some of the differences that one may expect to find should a Timoshenko beam model be used. Again, we use solutions obtained in Example 3 for 2×2 and 4×4 cells as a reference and compare the dispersion diagrams under Euler-Bernoulli and Timoshenko beam assumptions. The results are shown in Fig. 17.

The relaxation of the kinematic constraints introduced by the Timoshenko beam has a complex effect on

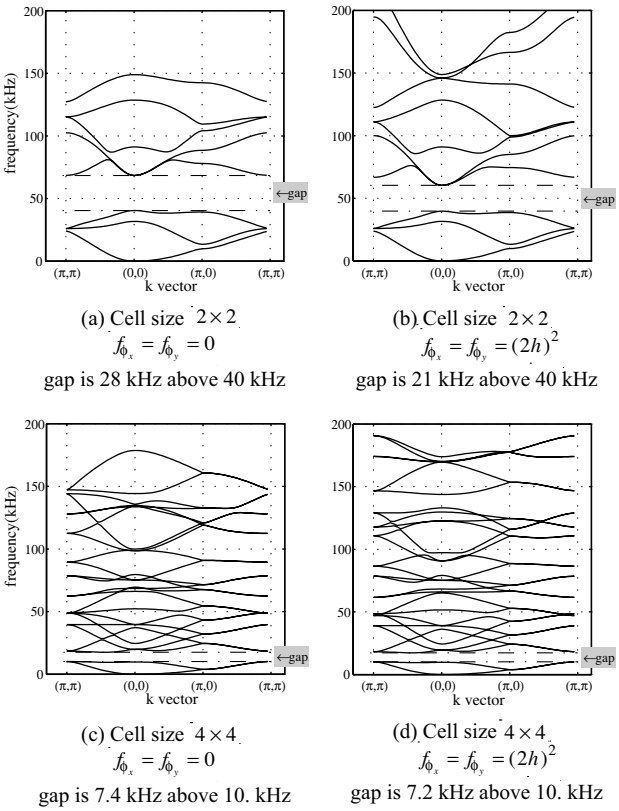

Fig. 16 The influence of rotational inertia on the dispersion diagrams

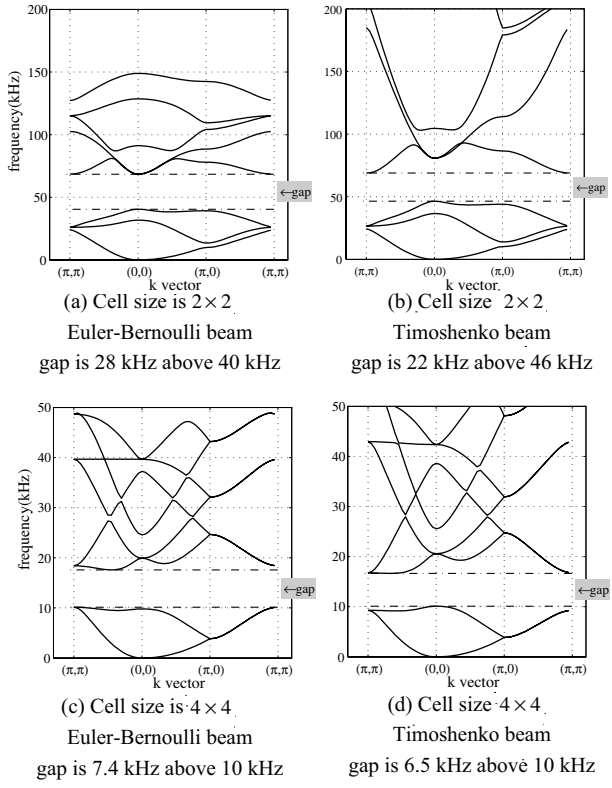

Fig. 17 Dispersion diagrams indicating the difference between using Euler-Bernoulli and a Timoshenko beam models

the solution at higher frequencies, which in this case results in a net reduction of the gap size. The effect is less significant at lower frequencies but there again the Timoshenko beam model has smaller band-gaps. It should be noted that as the mass distributions that result in the dispersion diagrams shown in Fig. 17(b) and (d) were not designed to be optimal under the Timoshenko beam assumptions, one may expect a small improvement if the mass distribution were optimized under the new modelling assumptions. However, in these examples one can show that the improvements obtained by further optimization are not significant.

6.6

Example 6. Finite size solutions

The designs performed in the previous sections are based on the assumption that the grid is infinitely periodic along both tiling vectors. In practice, however, any implementation will involve only a finite - possibly small - number of cells. Here we investigate whether a grid of finite size behaves as an infinitely-periodic medium. The results show that even a patch made of a relatively small number of cells exhibits a frequency response similar to the one predicted by the periodic analysis, provided that the response is measured some distance away from the boundary, to avoid edge effects. Experience indicates that boundary conditions may introduce modes with frequencies within the gap, but these modes are highly localized to the edges of the domain.

Square patches of 4×4 cells designed to have a maximum gap above the second band (see Fig. 10(c) and Fig. 11(c)) are built using either 6 or 12 cells per side. A spatially random, time periodic, transverse load is applied to all nodes of the patch, which is simply supported at the edges. The response is monitored everywhere in a square area centered on the patch center and extending halfway towards the edge in all directions. The maximum amplitude of the response A within the monitored area is reported for each frequency of the input force. The response is normalized with respect to the static response, $A0$.

The frequency response curve for the smaller, 6×6 patch is shown in Fig. 18(a). The figure shows there is little response when the forcing frequency is in the gap range. Fig. 18(b), corresponding to a larger, 12×12 patch, show an even more significant attenuation of the response. This validates the notion that finite size implementations of designs obtained from infinitely periodic analysis do exhibit properties similar to their infinitely periodic counterparts.

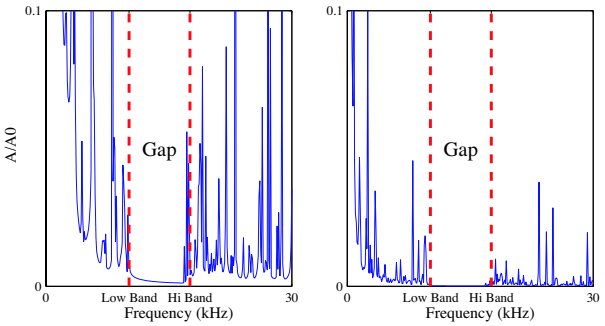

(a) 4×4 patch (b) 12×12 patch

Fig. 18 Frequency response for simply supported patches of cells designed to have a gap in the range [10.1,17.5] (Fig. 10(c) and 11(c))

7 Conclusions and discussion

A variety of examples demonstrate different strategies to design band-gaps into a plane grid structure. The sensitivity of the gap width and its position relative to different bands has been studied with respect to the addition of non-structural masses. Solutions are found to be related to specific critical points in the dispersion diagram. Typically, these points are at values of the wave vector associated with standing waves in the structure. An understanding of the sensitivity of the gap width to the mass position can be gained by studying the modes at these critical points. The influence of the skew angle of the grid on the distribution of the bands has also been reported. The relationship between this angle, the width of the band-gap, and the inter-band positioning has been numerically investigated and the complexity of this relationship was demonstrated. Clearly, this angle could be employed as another design parameter in the optimization scheme, but this was not detailed in the current study. However, some effects of the underlying mathematical modelling of the structure were investigated. For instance, it was observed that the difference between an Euler and a Timoshenko beam model was more significant at the higher frequencies. The effect of including rotational inertia to the non-structural masses was also shown to influence the higher frequencies. This latter effect could be employed as a design variable as the construction of the actual structure might be chosen to allow this quantity to be varied in an real design.

A novel way of viewing the scaling issue of the reference cell was discussed. The relationship between small, irreducible cells and larger, reducible cells was presented. Exploiting this relationship so that only a low number of bands at the lower frequencies need be considered when trying to position a gap can lead to a reduction in the level of complexity of the system to be optimized. A sequence of 1×1 , 2×2 , and 4×4 reference cell sizes where used to numerically demonstrate this observation.

The majority of the reported work dealt with periodic structures of infinite size, but to demonstrate the validity of the results to more practical finite systems, examples of frequency response functions were generated for structures consisting of a small number of cells. These clearly showed that little or no frequencies could pass through the structure in the region of the band-gap.

All results reported here are only local optima, verified after re-starting the optimization scheme from many random starting points. There are many numerical issues that could be addressed more efficiently by improved optimization algorithms, specially tailored for this problem. There is much room for improvement in this area.

Work is continuing to prove rigorously that only a very limited number of critical wave vectors need be explored to ensure that optimal solutions have been located. Moreover, results reported here suggest that the sensitivity variation with respect to the distribution of the design variables (whether it be mass, skew angle, cross sectional dimension ratio of the beam elements, etc) can be guided by the standing waves that are associated with the critical wave vectors. This promises to be a fruitful avenue for future research and could lead to vast simplifications in the overall optimization scheme.

Acknowledgements The implementation of the method of moving asymptotes used here was provided by Prof. Krister Svanberg from the Department of Mathematics at KTH in Stockholm. We thank Prof. Svanberg for allowing us to use his program. The authors enjoyed many fruitful and intense discussions with Profs. Ole Sigmund and Jakob Jensen from DTU during the preparation of this manuscript. This work was supported in part by the U.S. National Science Foundation through Grant DMI 9912520 (AD). This support is gratefully acknowledged.

References

Brillouin, L. 1953: *Wave propagation in periodic structures.* 2nd edition, New York: Dover Publications Inc.

Cox, S.J.; Dobson, D.C. 2000: Band structure optimization of two-dimensional photonic crystals in H- polarization, *Journal of Computational Physics* 158, 214–224.

Cox, S.J.; Dobson, D.C. 1999: Maximizing band-gaps in two-dimensional photonic crystals, *SIAM J.Appl. Math.* 59, 2108–2120.

Diaz, A; Benard, A. 2001: On The Discretization Of Problems Involving Periodic Planar Tilings, *Communications in Numerical Methods in Engineering*, 17, 543–549.

Dowling J. and Everitt H. 2004: Sonic Band-Gap Bibliography, http: // home.earthlink.net /∼jpdowling/ pbgbib.html

Heckel, M.A. 1964: Investigations on the vibrations of grillages and other simple beam structures, *Journal of the Acoustical Society of America* 36, 1335–1343.

Jensen, J.S. 2003: Phononic band-gaps and vibrations in one-and two-dimensional mass-spring structures, *Journal of Sound and Vibration* 266, 1053–1078.

Kafesaki, M., Sigalas, M. M., Economou, E. N. 1995: Elastic wave band-gaps in 3-D periodic polymer matrix composites, Solid State Communications 96 (5), 285–289.

Langlet, P.; Hladky-Hennion, A.-C.; Decarpigny, J.N. 1995: Analysis of the propagation of plane acoustic waves in passive periodic materials using the finite element method, *Journal of the Acoustical Society of America* 98, 2792–2800.

Ma, L.; Diaz, A.; Haddow, A. 2004: Modeling and design of materials for controlled wave propagation in plane grid structures, Paper DETC2004-57183, *Proc. of DETC'04, ASME 2004 Design Engineering Technical Conf.* , Salt Lake City, UT.

Martinsson, P.G.; Movchan, A.B. 2003: Vibrations of lattice structures and phononic band-gaps, *Q.Jl Mech. Appl. Math.* 56 (1), 45–64.

Orris, R.M.; Petyt, M. 1974: A finite element study of harmonic wave propagation in periodic structures, *Journal of Sound and Vibration* 33, 223–236.

Sigalas, M.; Economou, E. 1994: Elastic waves in plates with periodically placed inclusions, *Journal of Applied Physics*, 75(6), 2845–2850.

Parmley, S.; Zobrist, T.; Clough, T.; Perez Miller,A.; Makela, M.; Yu, R. 1995: Phononic band structure in a mass chain, *Appl. Phys. Lett.* 67 (6), 777–779.

Sigmund, O. 2001: Microstructural design of elastic band-gap structures, *Proc. of the Second World Congress of Struct. and Multidisc. Optim.* . Dalian, China.

Sigmund, O.; Jensen, J.S. 2002: Topology optimization of phononic band-gap materials and structures, *Fifth World Congress on Computational Mechanics*. Vienna, Austria.

Sigmund, O.; Jensen, J.S. 2003: Systematic design of phononic band-gap materials and structures by topology optimization, *Phil. Trans. R. Soc. Lon. A* 361, 1001–1019.

Svanberg, K. 1987: The method of moving asymptotes. *Int.J.Num. Mech. Eng.* 24,459–373.

Vasseur, J.O.; Deymier, P.A.; Frantziskonis, G.; Hong, G.; Djafari-rouhani, B.; Dobrzynski, L. 1998: Experimental evidence for the existence of absolute acoustic band-gaps in two-dimensional periodic composite media, *Journal of Physics: Condensed Matter* 10, 6051–6064.